THE JOURNAL OF PHYSICAL CHEMISTRY C

Article

Cite This: J. Phys. Chem. C 2019, 123, 4168–4177

pubs.acs.org/JPCC

Electronic Structure Tunability of Diamonds by Surface Functionalization

Gary Wan,[†,‡] Mattia Cattelan,*[,§] and Neil A. Fox[†,§]

[†]School of Physics, HH Wills Physics Laboratory and [‡]Bristol Centre for Functional Nanomaterials, University of Bristol, Tyndall Avenue, Bristol BS8 1TL, U.K.

[§]School of Chemistry, University of Bristol, Cantocks Close, Bristol BS8 1TS, U.K.

Supporting Information

ABSTRACT: Wide-bandgap semiconductors are exploited in several technological fields such as electron emission devices, energy conversion, high-power high-temperature electronics, and electrocatalysis. Their electronic properties vary significantly depending on the functionalization of the surface. Here, we investigated as a proof-of-concept the modulation of the electronic properties of one of the most common wide-bandgap semiconductors, that is, diamonds, to show the tunability of their properties by modifying the surface termination. Photoelectron spectroscopy was used to demonstrate the availability of a wide window of band bending, work function, and electron affinity. The band bending and work function were found to change by up to 360 meV and 2 eV, respectively, by varying the surface from hydrogen- to oxygen-terminated. Because of the negative electron affinity of diamonds, we were able to experimentally show the rigid shift of the whole band structure.

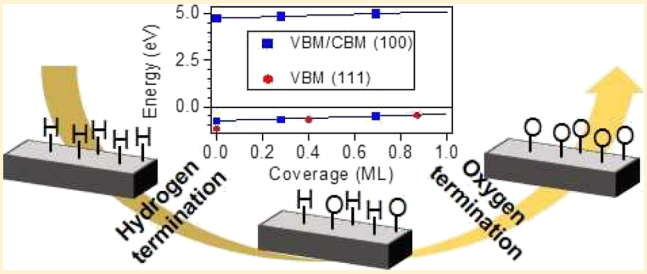

INTRODUCTION

Modification of the band structure of wide-bandgap materials is of fundamental importance for many applications, such as surface transfer doping,[1−3] thermionic electron emission,[4] light-emitting devices,[5,6] and high-power high-temperature electronics.[7] Some wide-bandgap materials, such as diamonds, with their robustness and favorable electronic properties, are also used in electrochemistry and electrocatalysis.[8,9] One effective and simple way to modify the band structure of a diamond is to alter its surface termination. Indeed, the effect of surface functionalization and orientation of a diamond has been studied extensively in the past,[10−19] where the band bending, negative electron affinity (NEA), and work function (WF) were compared between hydrogen- and oxygen-terminated samples. The aim of the current study is to build on past work in the literature with innovative characterization techniques and prove the tunability of diamond properties.

The surface termination has a major role in the reactivity and performance at the diamond interface.[20,21] For instance, in electrocatalysis, platinum (Pt) nanoparticles supported on oxygen-terminated diamond powders were shown to exhibit higher catalytic conversion efficiency for methanol and formic acid oxidation, compared with Pt nanoparticles on hydrogen-terminated diamond powders.[22] However, hydrogen-terminated diamond surfaces showed favorable performance in photocatalytic reduction and photochemical functionalization over oxygen-terminated surfaces.[23,24] These contrasts were attributed to the large differences in surface dipoles of the hydrogen- and oxygen-terminated diamond surface, and thus the different shifts in electronic structure. Tuning these surface electronic properties will enable the performance optimization of such devices.

Some wide-bandgap semiconductors have a peculiar property called NEA, where the vacuum level at the surface lies below the conduction band minimum (CBM), allowing for a significantly reduced barrier for electron emission. Hydrogen-terminated diamond surfaces exhibit NEA,[12] which is a fundamental feature for thermionic devices,[25] photon detectors, and cold cathode emitters,[26] but is unstable at high temperatures and thus make it impractical for high-temperature applications such as in thermionic energy converters.[27] GaN and AlN can exhibit an NEA surface with a Cs−O termination,[28] and some metal oxide terminations on diamonds[14,15] are able to exhibit NEA behavior with a higher thermal stability. The careful characterization of the oxygen surface is useful for optimizing the oxygen termination procedure and understanding its effects on the electronical, chemical, and physical surface properties, and is pivotal for the growing interest in metal oxide terminations.[14,15,26,28]

Here, in order to study the surface functionalization of diamonds in an innovative way, the two most common diamond surfaces, fully hydrogenated (100) and (111) diamond surfaces were characterized under ultrahigh vacuum (UHV) conditions while gradually increasing oxygen coverage. The state-of-the-art

Received: November 20, 2018
Revised: January 26, 2019
Published: January 28, 2019

DOI: 10.1021/acs.jpcc.8b11232
J. Phys. Chem. C 2019, 123, 4168–4177

surface science techniques we used here are as follows: energy-filtered photoemission electron microscope (EF-PEEM) in real and reciprocal spaces, spot profile analysis low-energy electron diffraction (SPA-LEED), X-ray and ultraviolet photoelectron spectroscopy (XPS, UPS).

EF-PEEM allowed us to obtain high-energy and lateral-resolution photoemission imaging in real space, and full wavevector angle-resolved photoemission spectroscopy (ARPES) in reciprocal space, throughout the oxygen termination process. To the best of the authors' knowledge, these techniques have not been used before on diamond surfaces. Photoemission imaging by PEEM gives surface characterizations with energy resolution in the range of tens of mega-electron volts and lateral resolution in the order of tens of nanometers, respectively. It has been exploited for several materials[29−34] but its potential, especially in the reciprocal space,[35] has still not yet been fully explored. Importantly, PEEM electronical and WF contrasts were successfully used to follow chemical and catalytic reaction kinetics,[36−39] and for probing intercalation mechanisms on graphene.[40,41] In this work, the WF contrast has been used to monitor the changes during the replacement of hydrogen with oxygen functionalization and to carefully select the areas for UPS. ARPES is one of the few techniques that has the energy and reciprocal space resolution needed to visualize a material's band structure.[42−44] Full wavevector ARPES has been used to study the electronic state of graphene[45−47] and transition-metal dichalcogenides,[35] and is crucial for orbital tomography.[48] In this work, it has been exploited to precisely find the valence band maximum (VBM) by selecting only the features at Γ.

The range of surface science techniques used here allowed us to visualize step-by-step changes in the electronic and morphologic structure of the samples, and thus measure the intermediate stages of termination from hydrogen to oxygen termination. We proved the tunability of the sample electronic properties by establishing the relation between oxygen coverage and electronic properties of diamonds, taking a fundamental step forward from previous literature works.[10−19] Our findings are also a stepping stone for future EF-PEEM in-operando studies where semiconductors are investigated as functions of time, position, and applied electric field.[49−51] The possibility to tune the electronic properties of diamonds by modifying the surface functionalization is also a proof-of-concept demonstration applicable to other wide-bandgap materials.[52−54]

METHODS

Diamond Preparation. Two conductive diamond films were produced by growing boron-doped layers onto (100) and (111) single-crystal diamond substrates purchased from Element Six (145-500-0248 and MM 111/4010). Growth was done in an Applied Science and Technology (ASTeX)-type microwave plasma-enhanced chemical vapor deposition (CVD) reactor for 10 min, using 3% CH_4 and 3 ppm B_2H_6 in H_2. The (100) layer was grown at 1400 W and 140 Torr, at a temperature ranging between 950 and 980 °C. The (111) was grown at 1300 W and 130 Torr, at a temperature between 960 and 990 °C. Both samples were then immediately hydrogen-terminated after growth with a pure hydrogen plasma at 900 °C for 2 min, followed by 2 min at 500 °C.

The two hydrogen-terminated (100) and (111) samples were then transferred into the Bristol NanoESCA Facility's UHV chambers, where they were subsequently annealed at 300 °C under UHV conditions for 1 h for surface cleaning.

Surface Science Experiments. XPS was performed using a monochromatic Al Kα source (1486.7 eV), with the analyzer at 45° to the normal sample. A pass energy of 20 eV was used, for an overall energy resolution of 600 meV.

SPA-LEED was used to investigate the surface reconstruction and roughening of the samples.

A NanoESCA II EF-PEEM was used for full wavevector ARPES,[35] WF mapping, and region-selected UPS. A high-intensity focused and fully monochromatized He−I UV source (21.2 eV) was used as the excitation source. The lateral resolution of the WF map was less than 150 nm.

Oxygen dosing was performed by exposing the samples to an oxygen cracker in a total pressure of 2×10^{-6} mbar of oxygen at room temperature for a set amount of time, after which the samples were characterized again using the techniques mentioned above. This procedure was repeated multiple times for a total oxygen dosage duration of 130 min.

Density Functional Theory Modeling. Density functional theory (DFT) using the Perdew−Burke−Ernzerhof approximation[55] was used to calculate electric potentials through the diamond surfaces with the CAmbridge Serial Total Energy Package (CASTEP).[56] Plane waves of up to 900 eV were used as the basis set to construct the electron density, with pseudopotentials to eliminate core electrons from the calculation.[57] For the (100) surface, a 5.05 Å × 2.52 Å × 30 Å supercell was used, allowing for a 2 × 1 reconstructed slab of 10 layers of 2 carbon atoms, where a Monkhorst and Pack (MP) grid of 7 × 14 × 1 *k*-points was sufficient to sample the Brillouin zone.[58] A hexagonal supercell for the (111) surface of side length 2.52 Å and height 21.8 Å was used, with a diamond slab 10 carbon layers thick, where an MP grid of 14 × 14 × 2 was used to sample the Brillouin zone. For both surface orientations of the single crystal diamond slabs, both sides were terminated with either a layer of hydrogen or oxygen.

RESULTS AND DISCUSSION

Photoemission Measurements and DFT Calculations. Here, we report XPS, UPS, ARPES, and WF data that have been acquired after each step of oxygen exposure using an oxygen cracker. The core-level photoemission gave us an indication of the quantity of oxygen adsorbed onto the surface and the dipole strength because of the surface transformation. UPS and ARPES provided information on the electron affinity and band bending of the top few atomic layers of the sample, whereas the WF maps allowed us to visualize the transformation from the hydrogen- to oxygen-terminated surface. The results are corroborated by DFT calculations.

XPS surveys done at each oxygen-dosing step show no indication of contamination from the cracker filament, and only carbon and oxygen peaks were present. For both the (100)- and (111)-orientated samples, the C 1s peak decreased, whereas the O 1s line increased with oxygen-cracking duration, from the attenuation of signal because of the replacement of hydrogen on the diamond surface with oxygen. Figure 1 shows the stoichiometry of the carbon and oxygen signals of both samples, normalizing the photoemission line areas by their sensitivity factors. This was plotted with respect to oxygen exposure time and no clear saturation point was observed even after 130 min.

The absence of a clear plateau in the O−C ratio can be explained by the roughening of the diamond surface from atomic oxygen exposure, increasing the surface area for oxygen adsorption. Oxygen has been used to enhance diamond CVD growth,[59,60] and oxygen ions are known to slowly etch diamond

DOI: 10.1021/acs.jpcc.8b11232
J. Phys. Chem. C 2019, 123, 4168−4177

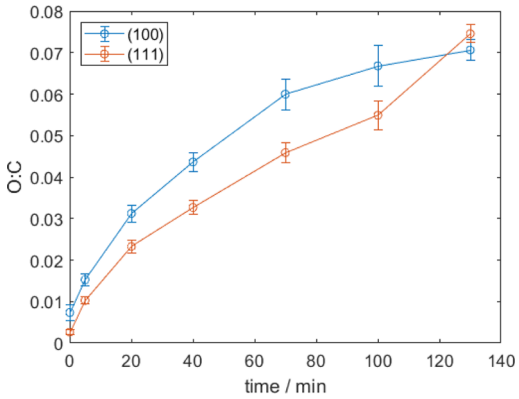

Figure 1. Oxygen to carbon signal ratio from XPS with respect to oxygen-cracking duration. The (100)- and (111)-orientated samples are represented in blue and orange, respectively.

surfaces.[61,62] Atomic oxygen exposure at room temperature shows similar behavior by deteriorating the diamond surface, as seen by Shpilman et al. using the afterglow of an oxygen plasma for atomic oxygen.[63]

The C 1s and O 1s XPS spectra after each step for the (100) and (111) surfaces are shown in Figure 2.

Initial core-level spectra for both the hydrogen-terminated surfaces were similar, with a binding energy of 284.4 eV for the C 1s peak from the boron-doping,[64] and 532.6 eV for the O 1s peak, which may have come from small defects of the single crystals (the quantity of oxygen is <1 at. % for the hydrogen-terminated crystals). After the first 5 min of oxygen cracking, both C 1s peaks of the two surfaces shifted to higher binding energies, similar to the reported C 1s core level of oxidized diamond surfaces.[65] The (100) C 1s core level stopped shifting after the first 5 min, whereas the O 1s peak continually decreased in binding energy with oxygen dosing. Meanwhile, for the (111) surface, the O 1s binding energy remained constant with oxygen cracking, whereas the C 1s peak continually increased in binding energy.

The binding energy shift, asymmetry, and broadening of the C 1s peak have been attributed to surface band bending and surface state formation in the past,[10] though those may not be the only contribution to such effects. Indeed, with our step-by-step acquisitions we observed a complex trend of shifting and broadening of the C 1s peaks in Figure 2 for both the (100) and (111) surfaces. We believe these are the result of complex phenomena which include, not exclusively, surface state formation and band bending, but also surface roughening as discussed below.

The shifting of oxygen and carbon core-level binding energies occurs in opposite directions, and their relative shifts in binding energy after each oxygen-cracking step are plotted in Figure 3, where ΔBE is the difference between the C 1s and O 1s shifts in binding energy. A saturation of the shifts in binding energy is observed, which would indicate when a full oxygen coverage is obtained.

For both the (100)- and (111)-orientated samples, their relative C 1s and O 1s shifts are similar, which can be explained by the dipole formation induced by the oxygen on the surface of

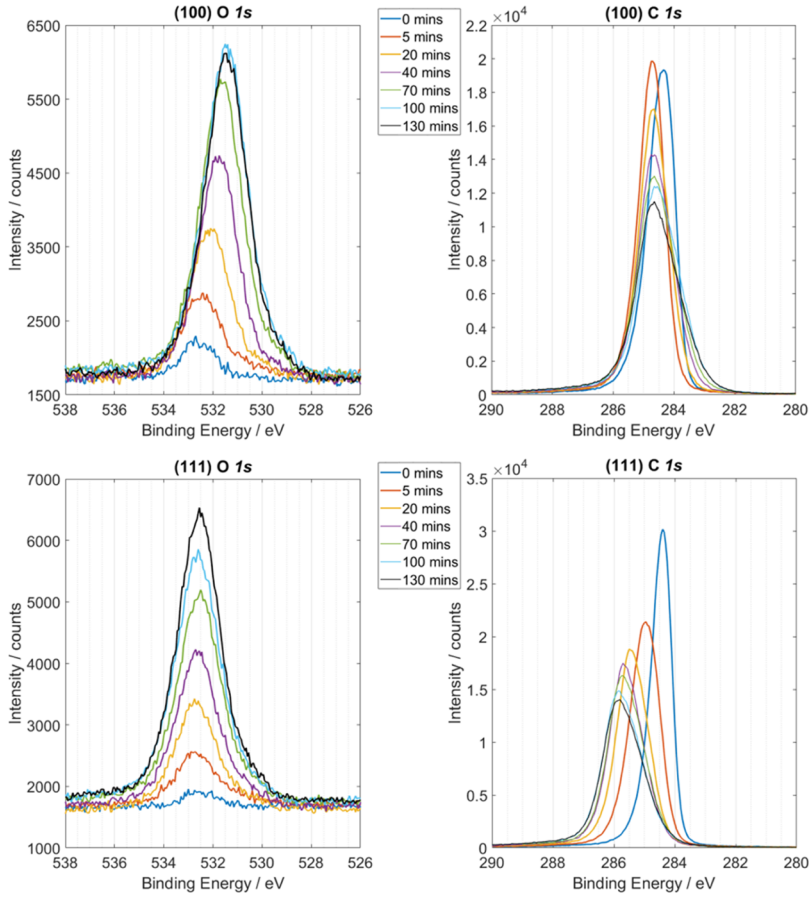

Figure 2. XPS spectra of O 1s (left) and C 1s (right) peaks of the (100) (top) and (111) (bottom) surfaces after each step of oxygen cracking.

DOI: 10.1021/acs.jpcc.8b11232
J. Phys. Chem. C 2019, 123, 4168−4177

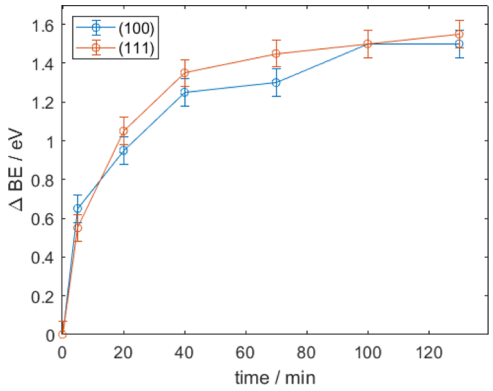

Figure 3. Shift in binding energies between the C 1s and O 1s XPS spectra with respect to oxygen-cracking duration. The (100) and (111) surfaces are shown in blue and orange, respectively.

the diamond.[13] The electric potential at the surface of the hydrogen- and oxygen-terminated sample is therefore significantly different. Oxygen has a higher electronegativity than carbon, so the surface carbon atoms bonded with oxygen have a slight positive charge, whereas the oxygen atoms possess a slight negative charge.[16] This forms a dipole on the surface of the diamond, where the surface oxygen atoms will be on the negatively charged side of the dipole, whereas the layer of carbon underneath will be on the positive side. Therefore, the O 1s spectra will be shifted to lower binding energies (or higher kinetic energy) because of the increased electric potential on the oxygen atoms, whereas the opposite occurs for the carbon atoms directly below the surface.[14] The difference in energy shifts between the C 1s and O 1s peaks goes up to 1.5 eV after 130 min of oxygen exposure, and it gives an indication of the dipole moment formed between the carbon and oxygen layers.

While the relative shifts in the C 1s and O 1s binding energies are found to be the same for both (100) and (111) diamond surfaces, it is unclear why on the (111) surface the C 1s peak shifts in energy, whereas the O 1s energy stays fixed, whereas the opposite occurs for the (100) surface. We therefore did DFT calculations to help understand these phenomena. Figure 4 shows the electrostatic potential through the two diamond surfaces for hydrogen and oxygen terminations from DFT calculations. The plots were aligned between the two different terminations by their bulk potentials for easier comparison, as the electric potential at each atom's position can then be directly linked to the binding energies in XPS. The final binding energy shift for carbon in Figure 2 should be closely related to the change of $V_{surface}$ relative to V_{bulk} from a hydrogen to oxygen termination.

From the data used to generate Figure 4, we would expect the shift in binding energy of carbon after oxygen termination to be −0.04 eV for the (100) surface and +1.25 eV for the (111) surface, compared to the +0.5 and +1.5 eV from the XPS in Figure 2. The difference in values could have been from insufficient datapoints in the electric potential plot, making it difficult to determine the potential at a precise position. However, the results qualitatively confirm that the carbon peak shifts significantly less for the (100) than the (111) surface. The DFT calculation showed a significantly larger oscillation of potential through the (111) surface, making it incomparable with the (100) surface; otherwise, the binding energy shift in oxygen peak could also be compared with experimental values.

The surface dipole is also responsible for the change in electron affinity of the diamond samples, where a hydrogen-terminated surface exhibits an NEA[12] because of its lower electronegativity than carbon, whereas the oxygen-terminated surface has a positive electron affinity. Therefore, the change from a hydrogenated to oxygenated diamond surface will also have a significant effect on the WF, which is shown in Figure 4 by the noticeably higher electric potential at the vacuum level for the oxygen-terminated diamond than the hydrogen-terminated one.

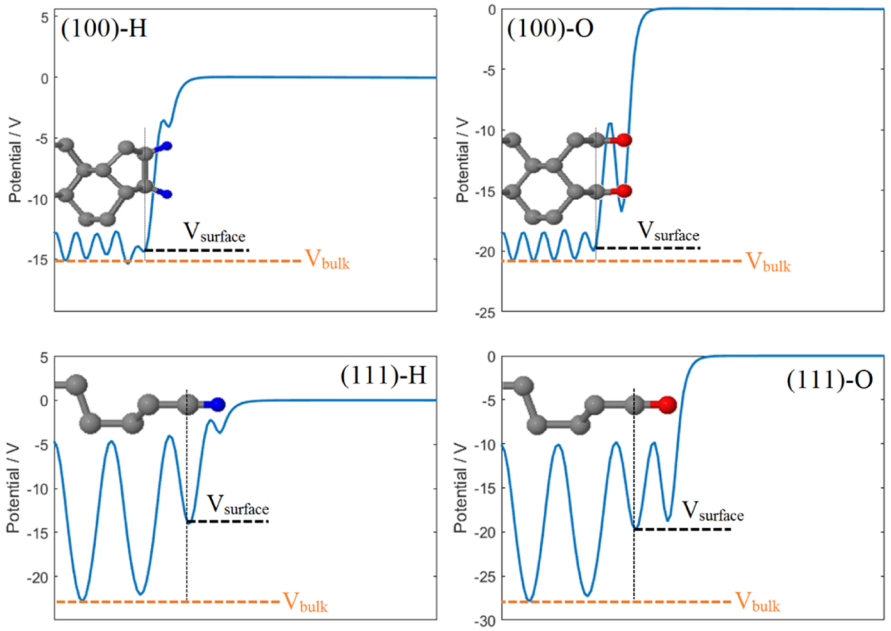

Figure 4. DFT calculations for electric potentials of the (100) (top) and (111) (bottom) diamond with hydrogen (left) and oxygen (right) terminations. Carbon atoms are in gray, whereas hydrogen and oxygen are in blue and red, respectively. The *y*-axis for the hydrogen-terminated surface is shifted downwards to align with the V_{bulk} of the oxygen-terminated surface.

DOI: 10.1021/acs.jpcc.8b11232
J. Phys. Chem. C 2019, 123, 4168−4177

Region-selected UPS of the samples after each step of oxygen cracking are shown together in Figure 5, where the area of interest was selected using an EF-PEEM mechanical aperture. The advantage of this over-conventional UPS[10,11,13,18,66] is the ability to avoid macroscopic defects on the sample that can affect the acquisitions. The existence of macro-defects is suggested by the oxygen contamination on the fully hydrogenated samples as seen in Figure 2. The spectra were produced using a monochromatic 21.2 eV He−I source. The x-axis represents the energy of the detected electron, relative to the Fermi level (E_f) of the sample.

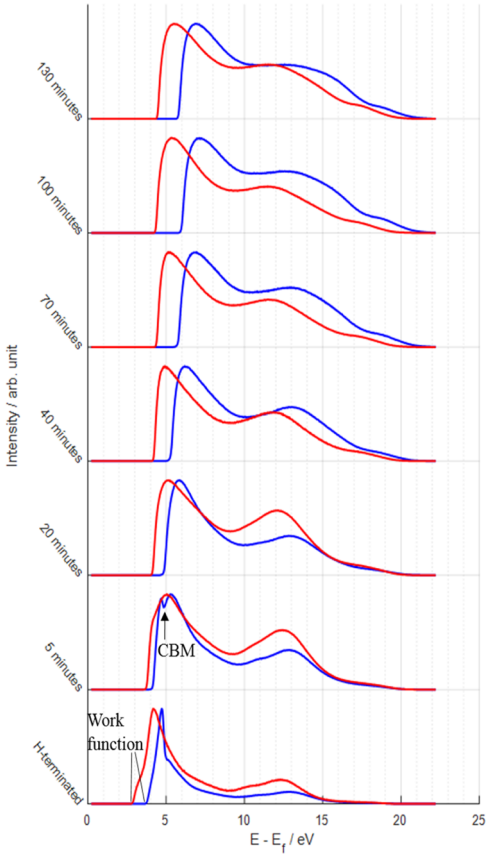

Figure 5. Selected area UPS spectra of the (100) (blue) and (111) (red) surfaces after oxygen-cracking steps. The spectra are normalized and shifted vertically for clarity.

During the UV photoemission process, electrons in the valence band are photoexcited to higher electronic states in the conduction band, where they can be directly emitted into the vacuum or thermalize to lower-energy states before emission. When using a monochromatic photon source, the fastest electrons detected can be used to determine the VBM position. On the low-energy end of the spectra, the cutoffs give the vacuum level (therefore WF) of the sample,[67] which increases with the oxygen-cracking duration because of the higher electron affinity induced by oxygen. From Figure 5, the hydrogen-terminated surfaces had an initial WF between roughly 3 and 4 eV, which then gradually increased with oxygen exposure. At high oxygen exposure durations, we noticed an additional feature appear at about 3 and 4 eV of binding energy for the (100) and (111), respectively. This is attributed to an oxygen-induced surface state as previously reported by Loh.[17,18]

As the hydrogen-terminated diamond surfaces exhibit NEA, the vacuum level lies below the CBM; therefore, secondary electrons thermalized to the CBM can be emitted. As referred to by Diederich et al. as an NEA peak,[68] an intense peak starting at the CBM results because of the accumulation of relaxed electrons,[12] whereas electron emissions from below the CBM are associated with surface states within the band gap.[10]

In the UPS spectra of Figure 5, the low-energy peaks of the hydrogen-terminated sample and the sample after 5 min of oxygen exposure both have a broad shoulder that drops to zero intensity at the low-energy cutoff. As explained above, the broad peak arises from the contribution of relaxed electrons from both surface states as well as the CBM, with the CBM being the higher energy component. For the (100) hydrogenated surface and after 5 min of oxygen cracking (blue lines), the two peaks can be clearly distinguished, and the CBM is taken to be at the point where the second peak begins, at around 4.75 and 4.85 eV above E_f, respectively. ARPES was done at the higher-energy portion of the spectra to determine the valence band structure (see Figure 7 and Supporting Information Figure S1), allowing a more accurate determination of the VBM position over angle-selected UPS spectra.[10,13] The VBM was found to be at 0.75 and 0.65 eV below E_f, respectively. This gives us an experimentally obtained value of 5.5 eV for the band gap, very close to the expected value.[69] For the hydrogen-terminated (100) sample, the low-energy cutoff was approximately 3.7 eV above E_f, giving an NEA, that is, the difference between the low-energy cutoff and the CBM, of about −1 eV, in good agreement with the literature.[10,70] Thanks to the NEA, we are able to experimentally observe the rigid shift of the whole band structure of diamonds because of the oxygen termination and observed unoccupied states above the E_f by photoemission without complex pump−probe ARPES setups[71] or alkaline surface-doping.[72,73] After 20 min of oxygen exposure, the NEA peak is no longer clearly visible as the WF cutoff is too close to the CBM.

Similarly, the (111) crystal presents an NEA when hydrogen-terminated and after 5 min of oxygen cracker exposure. The CBM peak is broader and less defined than the (100) crystal; this observation is due to the indirect band gap of diamonds. The CBM lies at 0.76 of the distance from the center of the Brillouin zone to the edge along the ⟨100⟩ direction.[74] This means that electrons at the bottom of the conduction band for the (111) surface have a relatively large momentum parallel to the surface ($k_{||} \approx 0.95$ Å^{-1}), so electrons at the CBM must first scatter inelastically and alter $k_{||}$ before being emitted. The peak from the (111) CBM was still observed because of the angle-integrated analyzer used, which may not be detected with angle-selected analyzers used in previous studies of Diederich, et al.[10] Detailed angle-resolved acquisition about these phenomena for the (100) and (111) surfaces will be investigated in a separate paper.

Because of the broadened NEA peak, it is more difficult to understand the energy position of the CBM on the (111) surface; however, the trend of increasing VBM for oxygen exposure is confirmed, going from 1.18 eV below E_f for the hydrogen-terminated surface, to 0.68 eV for 5 min and 0.46 eV for 20 min of oxygen cracking (Figure S1).

The average WF can be estimated from UPS by extrapolation of the low-energy cutoff to the background, as was done in previous studies,[10,14,15] but did not provide insight into the uniformity of the surface. WF maps were generated with pixel-by-pixel fitting of EF-PEEM images, which to the authors' best knowledge has not been done before on diamonds and can show the mechanism of oxygen replacing hydrogen because of the WF

DOI: 10.1021/acs.jpcc.8b11232
J. Phys. Chem. C 2019, 123, 4168−4177

contrasts. Figure S2 shows the WF maps of the (100) and (111) diamond surfaces when hydrogen-terminated and after 130 min of oxygen exposure. The WF was found to increase uniformly throughout each oxygen-cracking step as no noticeable formation of high WF islands were seen with a lateral resolution better than 150 nm, and there was also no evidence of macroscopic etching. The average WF values were obtained from the WF maps after each oxygen-cracking step by taking a homogenous region of interest and plotting the average values against oxygen-cracking duration (Figure 6). Interestingly, the

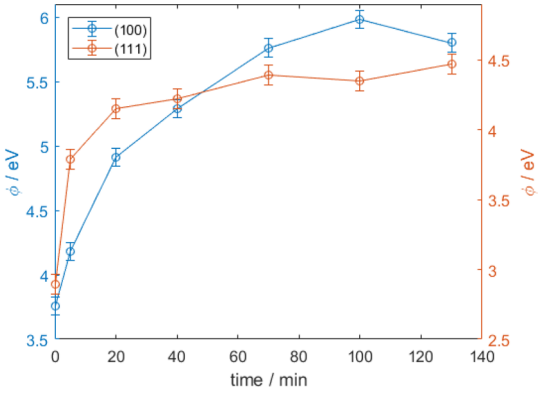

Figure 6. WF changes with respect to the oxygen exposure duration for the (100) (blue) and (111) (orange) diamond surfaces. The (111) WF is plotted on a separate *y*-axis for easier comparison.

(111) surface had a sharper increase in WF after 5 min of oxygen cracking compared to the (100) surface but saturates near 4.5 eV, whereas the (100) surface saturates at around 6 eV. Saturation begins after approximately 70 min of oxygen cracking for both samples.

ARPES was done on the samples near the top of the valence band to accurately determine the changes in surface band bending because of oxygen (see discussion above), similar to what has been done in the past;[42−44] however, the full wavevector ARPES allows for a more precise determination of VBM reciprocal space position compared to conventional UPS and ARPES setups. Figure 7 shows a full wavevector ARPES of the VBM for the hydrogen-terminated (100) and (111) samples. The intensity at the center of ARPES was plotted against binding energy, and the position of the VBM was determined to be where the signal dropped to the background level. The VBM for the hydrogen-terminated (100) and (111) surfaces was found to be at 0.75 and 1.2 eV binding energy, respectively, indicating a downward band bending. This was obtained assuming a boron-doped diamond with a bulk Fermi level of 0.25−0.3 eV above the VBM, as calculated by Bandis and Pate for diamonds with different boron concentrations.[10,75]

After oxygen exposure, the signal-to-noise ratio dropped significantly, leading to difficulty in finding the VBM position. Slices through energy along $k_{\parallel}$ (orange dotted line) in Figure 7 revealing the band structure of the crystals are reported in Figure S1. The samples showed an increase in upward band bending after 5 min of oxygen exposure, meaning that near the surface, an electric field drives the electrons into the bulk, thus generating more holes and causing the VBM to move upwards toward the Fermi level.

The decrease in the signal-to-noise ratio with oxygen exposure is predicted to be due to surface roughening of the samples from oxygen exposure. Figure 7 shows VBM ARPES images of both

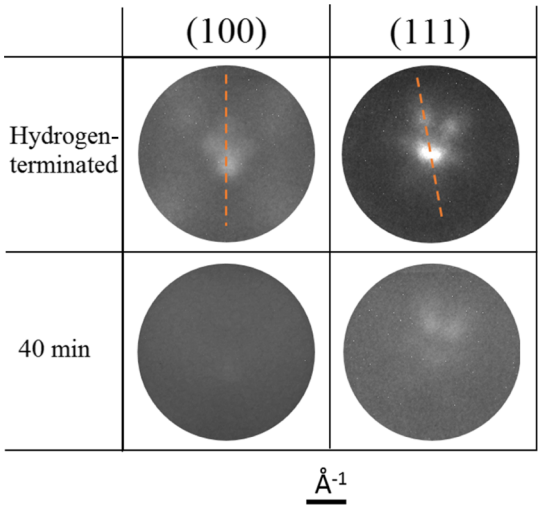

Figure 7. Full wavevector ARPES images of the (top) hydrogen-terminated (100) (left) and (111) (right) surfaces, and after 40 min of oxygen cracking (bottom). The images are integrated between 0 and 2 eV binding energy. The dotted lines are along $X-\Delta-X'$ for the (100) surface, and $K-\Lambda-K'$ for the (111).[76]

samples after 40 min of oxygen exposure, highlighting the increase in noise compared to hydrogen-terminated samples.

LEED Measurements. Diffraction with low-energy electrons has been employed to visualize the reconstruction on the surfaces and the roughening that occurs during the oxygen treatment. SPA-LEED was performed on the (100) sample with an electron energy of 100 eV, whereas 120 eV was used for the (111) sample. The hydrogen-terminated (100) surface forms a (2 × 1) reconstruction,[77] as shown in Figure 8. The (2 × 1)

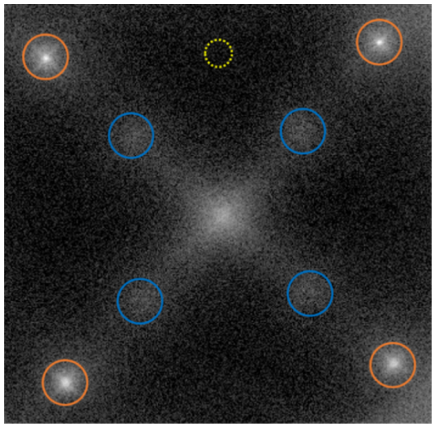

Figure 8. LEED pattern of the hydrogen-terminated (100) surface at 100 eV. The orange circles represent the (1 × 1) domain, blue is the (2 × 1) domain, and the yellow dotted circle was used as the background.

spots decreased in intensity with exposure to oxygen as the oxygen-terminated diamond (100) surface is (1 × 1) reconstructed, in agreement with Pehrsson and Mercer who also exposed a hydrogen-terminated (100) diamond surface to atomic oxygen and observed a (1 × 1) reconstruction.[77]

Spot profile analysis on the (100) LEED patterns after each oxygen exposure step was done by integrating the intensity around the (1 × 1) and (2 × 1) spots indicated by orange and blue circles in Figure 8, whereas the background was taken by integrating a spotless area (yellow dotted circle). Figure 9 shows

DOI: 10.1021/acs.jpcc.8b11232
J. Phys. Chem. C 2019, 123, 4168−4177

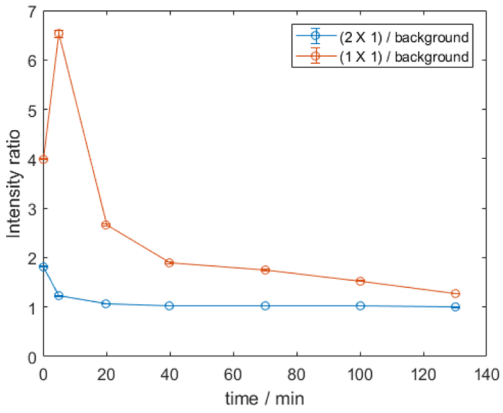

Figure 9. Intensity profiling of the (100) surface LEED pattern with respect to the oxygen-cracking duration. The signal intensity of the (2 × 1) and (1 × 1) spots divided by background are in blue and orange, respectively.

the intensity of the (1 × 1) and (2 × 1) patterns relative to background plotted against oxygen exposure time in orange and blue, respectively. The (2 × 1) ratio quickly decays with oxygen exposure because of the transition between the hydrogen (2 × 1) to oxygen (1 × 1) reconstruction.[77] However, the (1 × 1) ratio initially increased because of the favored reconstruction from oxygen replacement; it then begins to decay because of the rise in background. This ratio is not expected to drop for a surface with constant roughness, so the decay in signal is indicative of surface roughening, which agrees with our XPS and ARPES data.

The LEED pattern for the (111) sample showed a constant (1 × 1) reconstruction for the hydrogen- and oxygen-terminated surface as expected,[66,78] so spot analysis was done against the background in Figure S3. The intensity ratio for the (111) surface dropped significantly during the initial steps of oxygen cracking, indicating that roughening of the hydrogen-terminated surface from oxygen exposure occurs right away. The initial trend observed for the (100) surface in Figure 9 is different because of the increase in signal from the transition of (2 × 1) to (1 × 1) reconstruction.

Band Structure and Coverage. On the basis of our investigation, some observables reached a plateau with oxygen exposure as follows:

- Difference in binding energy shifts between C 1s and O 1s from surface dipoles (Figure 3)
- WF changes from the surface dipole (Figure 6)
- LEED intensity ratio of (1 × 1) spots versus background from surface roughening (Figures 9 and S3)

We proceed to fit such trends with exponential functions assuming that the surface is fully terminated after 130 min of oxygen exposure; then, we averaged the fitting to find a calibration for "oxygen exposure"/"oxygen coverage" as reported in Figure S4. Using this calibration curve, we can relate the oxygen exposure time to a coverage. For the (100), 5, 20, and 40 min correspond to a coverage of 0.24, 0.66, and 0.87 monolayers (ML) of oxygen, respectively, whereas for the (111), they correspond to 0.40, 0.87, and 0.96 ML. Interestingly, the (111) crystal reached the ML faster than the (100); we believe that this is strongly dependent on the surface preparation of the crystals.

We can now summarize the complete band diagram changes of the (100) crystal and the VBM trend of the (111) crystal from increasing oxygen coverage with a scheme and graph as presented in Figure 10.

We can observe that the band structure of the (100) shifts almost linearly from hydrogen to oxygen termination; a linear fit is added in Figure 10 to guide the eye.

The coverage calibration also helps with understanding the roughening of the surface after 40 min of exposure observed with XPS, ARPES, and LEED; the coverage after 40 min is so high (>0.9 ML of oxygen) that the reactive atomic oxygen begins etching the crystal, as previously found by Thomas et al. and Shpilman.[63,79]

CONCLUSIONS

We have demonstrated the possibility of modulating the WF and band structure of two diamond surfaces via simple control of oxygen adsorption onto a hydrogen-terminated surface and determined the relation between oxygen coverage and electronic properties. Carefully changing termination, the band bending can be tuned up to about 360 meV and the WF up to 2 eV. Shifts in core-level binding energies from XPS were explained by the dipole formation on the diamond surface, which also influenced the WF and the electron affinity of the samples. This type of analysis is important for future studies of bond and dipole strength and can be applied to more complex functional groups

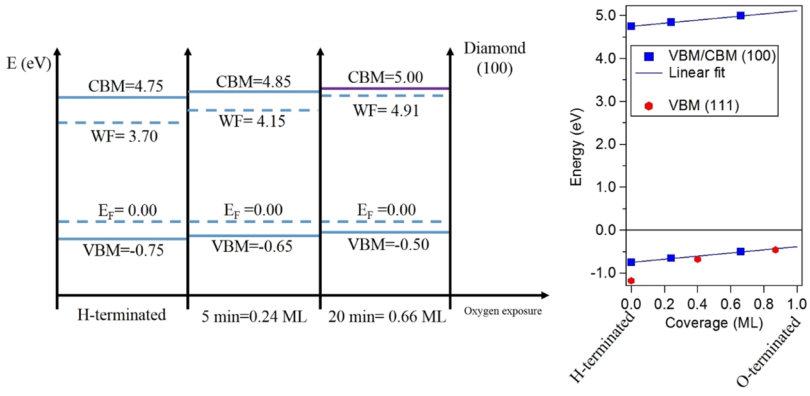

Figure 10. On the left, a scheme of the band bending of the (100) crystal because of the oxygen exposure. All the energy levels have been experimentally determined except for the CBM position of the sample after 20 min of oxygen exposure (purple) where a band gap of 5.5 eV has been assumed. On the right, the VBM and CBM of the (100) crystal are plotted as a function of the oxygen coverage in blue squares; the VBM trend of the (111) crystal is in red hexagons.

DOI: 10.1021/acs.jpcc.8b11232
J. Phys. Chem. C 2019, 123, 4168−4177

placed on diamond[14,15] and other materials.[52−54] EF-PEEM measurements showed that the oxygen adsorption occurs uniformly on a microscopic scale. Region-selected UPS and full wavevector ARPES allowed for an in-depth study of changes in surface band bending, with an important insight into unoccupied states above the Fermi level, using simple photoemission acquisitions.

Long exposure of a hydrogen-terminated diamond surface to atomic oxygen was found to cause surface roughening, which was observed from XPS, LEED, and ARPES analyses. This could be important information for the processing of diamond-based devices if the degradation of the surface hinders performance. Alternative oxygen-terminating procedures such as anodic polarization may potentially be used without such an effect.[20,21]

The surface band bending and changes in electron affinity are also prevalent in other wide-bandgap materials and play a key role in their performance in high-power and high-temperature electronic devices, thermionic application, and electrochemistry.[4−9] The ability to tune and predict these changes would greatly benefit development of the above applications.

■ ASSOCIATED CONTENT

Supporting Information

The Supporting Information is available free of charge on the ACS Publications website at DOI: 10.1021/acs.jpcc.8b11232.

ARPES of diamond (100) and (111) for hydrogen-terminated samples, after 5 and 20 min of oxygen exposure; WF maps of diamond (100) and (111) for hydrogen-terminated samples and after 130 min of oxygen exposure; SPA-LEED image and intensity ratio profile for diamond (111) versus oxygen exposure; coverage calculation for diamond (100) and (111) (PDF)

■ AUTHOR INFORMATION

Corresponding Author

*E-mail:mattia.cattelan@bristol.ac.uk. Phone: +44 (0)117 3940004.

ORCID

Mattia Cattelan: 0000-0001-9314-1475

Author Contributions

The article was written through contributions of all the authors. All the authors have given approval to the final version of the article.

Notes

The authors declare no competing financial interest.

■ ACKNOWLEDGMENTS

The authors acknowledge the Bristol NanoESCA Facility (EPSRC Strategic Equipment Grant EP/K035746/1 and EP/M000605/1). G.W. acknowledges the Ph.D. studentship funded through BCFN: Renewtec Technologies, Al Hamad Group.

■ REFERENCES

(1) Maier, F.; Riedel, M.; Mantel, B.; Ristein, J.; Ley, L. Origin of Surface Conductivity in Diamond. *Phys. Rev. Lett.* **2000**, *85*, 3472−3475.

(2) Hassan, M. M.; Larsson, K. Effect of Surface Termination on Diamond (100) Surface Electrochemistry. *J. Phys. Chem. C* **2014**, *118*, 22995−23002.

(3) Long, R.; Dai, Y.; Yu, L. Structural and Electronic Properties of Oxygen-Adsorbed Diamond (100) Surface. *J. Phys. Chem. C* **2007**, *111*, 855−859.

(4) Koeck, F. A. M.; Nemanich, R. J.; Lazea, A.; Haenen, K. Thermionic Electron Emission from Low Work-Function Phosphorus Doped Diamond Films. *Diamond Relat. Mater.* **2009**, *18*, 789−791.

(5) Neumark, G. F. Wide Bandgap Light-Emitting Devices Materials and Doping Problems. *Mater. Lett.* **1997**, *30*, 131−135.

(6) Kaplar, R. J.; Allerman, A. A.; Armstrong, A. M.; Crawford, M. H.; Dickerson, J. R.; Fischer, A. J.; Baca, A. G.; Douglas, E. A. Review-Ultra-Wide-Bandgap AlGaN Power Electronic Devices. *ECS J. Solid State Sci. Technol.* **2016**, *6*, Q3061−Q3066.

(7) Chalker, P. R. Wide Bandgap Semiconductor Materials for High Temperature Electronics. *Thin Solid Films* **1999**, *343-344*, 616−622.

(8) Hupert, M.; Muck, A.; Wang, J.; Stotter, J.; Cvackova, Z.; Haymond, S.; Show, Y.; Swain, G. M. Conductive Diamond Thin-Films in Electrochemistry. *Diamond Relat. Mater.* **2003**, *12*, 1940−1949.

(9) Holt, K. B.; Ziegler, C.; Caruana, D. J.; Zang, J.; Millán-Barrios, E. J.; Hu, J.; Foord, J. S. Redox Properties of Undoped 5 Nm Diamond Nanoparticles. *Phys. Chem. Chem. Phys.* **2008**, *10*, 303−310.

(10) Diederich, L.; Küttel, O. M.; Aebi, P.; Schlapbach, L. Electron Affinity and Work Function of Differently Oriented and Doped Diamond Surfaces Determined by Photoelectron Spectroscopy. *Surf. Sci.* **1998**, *418*, 219−239.

(11) Diederich, L.; Aebi, P.; Ku, O. M.; Schlapbach, L. NEA Peak of the Differently Terminated and Oriented Diamond Surfaces. *Surf. Sci.* **1999**, *424*, L314.

(12) Himpsel, F. J.; Knapp, J. A.; VanVechten, J. A.; Eastman, D. E. Quantum photoyield of diamond(111)-A stable negative-affinity emitter. *Phys. Rev. B: Condens. Matter Mater. Phys.* **1979**, *20*, 624−627.

(13) Maier, F.; Ristein, J.; Ley, L. Electron Affinity of Plasma-Hydrogenated and Chemically Oxidized Diamond (100) Surfaces. *Phys. Rev. B: Condens. Matter Mater. Phys.* **2001**, *64*, 165411.

(14) O'Donnell, K. M.; Edmonds, M. T.; Ristein, J.; Tadich, A.; Thomsen, L.; Wu, Q.-H.; Pakes, C. I.; Ley, L. Diamond Surfaces with Air-Stable Negative Electron Affinity and Giant Electron Yield Enhancement. *Adv. Funct. Mater.* **2013**, *23*, 5608−5614.

(15) O'Donnell, K. M.; Edmonds, M. T.; Tadich, A.; Thomsen, L.; Stacey, A.; Schenk, A.; Pakes, C. I.; Ley, L. Extremely High Negative Electron Affinity of Diamond via Magnesium Adsorption. *Phys. Rev. B: Condens. Matter Mater. Phys.* **2015**, *92*, 035303.

(16) Cui, J. B.; Ristein, J.; Ley, L. Electron Affinity of the Bare and Hydrogen Covered Single Crystal Diamond (111) Surface. *Phys. Rev. Lett.* **1998**, *81*, 429−432.

(17) Loh, K. P.; Xie, X. N.; Yang, S. W.; Zheng, J. C. Oxygen Adsorption on (111)-Oriented Diamond: A Study with Ultraviolet Photoelectron Spectroscopy, Temperature-Programmed Desorption, and Periodic Density Functional Theory. *J. Phys. Chem. B* **2002**, *106*, 5230−5240.

(18) Zheng, J. Oxygen-Induced Surface State on Diamond (100). *Diamond Relat. Mater.* **2001**, *10*, 500−505.

(19) Lim, C. H. Y. X.; Zhong, Y. L.; Janssens, S.; Nesladek, M.; Loh, K. P. Oxygen-Terminated Nanocrystalline Diamond Film as an Efficient Anode in Photovoltaics. *Adv. Funct. Mater.* **2010**, *20*, 1313−1318.

(20) Duo, I.; Levy-Clement, C.; Fujishima, A.; Comninellis, C. Electron Transfer Kinetics on Boron-Doped Diamond Part I: Influence of Anodic Treatment. *J. Appl. Electrochem.* **2004**, *34*, 935−943.

(21) Hutton, L. A.; Iacobini, J. G.; Bitziou, E.; Channon, R. B.; Newton, M. E.; Macpherson, J. V. Examination of the Factors Affecting the Electrochemical Performance of Oxygen-Terminated Polycrystalline Boron-Doped Diamond Electrodes. *Anal. Chem.* **2013**, *85*, 7230−7240.

(22) Celorrio, V.; Plana, D.; Flórez-Montaño, J.; Montes de Oca, M. G.; Moore, A.; Lázaro, M. J.; Pastor, E.; Fermín, D. J. Methanol Oxidation at Diamond-Supported Pt Nanoparticles: Effect of the Diamond Surface Termination. *J. Phys. Chem. C* **2013**, *117*, 21735−21742.

(23) Zhu, D.; Zhang, L.; Ruther, R. E.; Hamers, R. J. Photo-Illuminated Diamond as a Solid-State Source of Solvated Electrons in Water for Nitrogen Reduction. *Nat. Mater.* **2013**, *12*, 836−841.
(24) Nichols, B. M.; Butler, J. E.; Russell, J. N.; Hamers, R. J. Photochemical Functionalization of Hydrogen-Terminated Diamond Surfaces: A Structural and Mechanistic Study. *J. Phys. Chem. B* **2005**, *109*, 20938−20947.
(25) Ryan Smith, J. Increasing the Efficiency of a Thermionic Engine Using a Negative Electron Affinity Collector. *J. Appl. Phys.* **2013**, *114*, 164514.
(26) Rougeot, H.; Baud, C. Negative Electron Affinity Photoemitters. *Advances in Electronics and Electron Physics*; Academic Press, 1979; Vol. *48*, pp 1−36.
(27) Su, C.; Lin, J.-C. Thermal Desorption of Hydrogen from the Diamond C(100) Surface. *Surf. Sci.* **1998**, *406*, 149−166.
(28) Wu, C. I.; Kahn, A. Negative Electron Affinity and Electron Emission at Cesiated GaN and AlN Surfaces. *Appl. Surf. Sci.* **2000**, *162-163*, 250−255.
(29) Renault, O.; Barrett, N.; Bailly, A.; Zagonel, L. F.; Mariolle, D.; Cezar, J. C.; Brookes, N. B.; Winkler, K.; Krömker, B.; Funnemann, D. Energy-Filtered XPEEM with NanoESCA Using Synchrotron and Laboratory X-Ray Sources: Principles and First Demonstrated Results. *Surf. Sci.* **2007**, *601*, 4727−4732.
(30) Hoffmann, P.; Mikalo, R. P.; Schmeißer, D. A Spectro-Microscopic Approach for Spatially Resolved Characterisation of Semiconductor Structures in PEEM. *Solid-State Electron.* **2000**, *44*, 837−843.
(31) Chandra, A. P.; Gerson, A. R. The Mechanisms of Pyrite Oxidation and Leaching: A Fundamental Perspective. *Surf. Sci. Rep.* **2010**, *65*, 293−315.
(32) Renault, O.; Brochier, R.; Roule, A.; Haumesser, P.-H.; Krömker, B.; Funnemann, D. Work-Function Imaging of Oriented Copper Grains by Photoemission. *Surf. Interface Anal.* **2006**, *38*, 375−377.
(33) Keyshar, K.; Berg, M.; Zhang, X.; Vajtai, R.; Gupta, G.; Chan, C. K.; Beechem, T. E.; Ajayan, P. M.; Mohite, A. D.; Ohta, T. Experimental Determination of the Ionization Energies of MoSe2, WS2, and MoS2 on SiO2 Using Photoemission Electron Microscopy. *ACS Nano* **2017**, *11*, 8223−8230.
(34) Xiong, G.; Shao, R.; Droubay, T. C.; Joly, A. G.; Beck, K. M.; Chambers, S. A.; Hess, W. P. Photoemission Electron Microscopy of TiO2 Anatase Films Embedded with Rutile Nanocrystals. *Adv. Funct. Mater.* **2007**, *17*, 2133−2138.
(35) Cattelan, M.; Fox, N. A Perspective on the Application of Spatially Resolved ARPES for 2D Materials. *Nanomaterials* **2018**, *8*, 284.
(36) Mu, R.; Fu, Q.; Jin, L.; Yu, L.; Fang, G.; Tan, D.; Bao, X. Visualizing Chemical Reactions Confined under Graphene. *Angew. Chem., Int. Ed.* **2012**, *51*, 4856−4859.
(37) Vogel, D.; Spiel, C.; Suchorski, Y.; Urich, A.; Schlögl, R.; Rupprechter, G. Mapping the Local Reaction Kinetics by PEEM: CO Oxidation on Individual (100)-Type Grains of Pt Foil. *Surf. Sci.* **2011**, *605*, 1999−2005.
(38) Prieto, M. J.; Schmidt, T. LEEM and PEEM as Probing Tools to Address Questions in Catalysis. *Catal. Lett.* **2017**, *147*, 2487−2497.
(39) Lovis, F.; Imbihl, R. Self-Organization of Ultrathin Vanadium Oxide Layers on a Rh(111) Surface during a Catalytic Reaction. Part I: A PEEM Study. *J. Phys. Chem. C* **2011**, *115*, 19141−19148.
(40) Jin, L.; Fu, Q.; Yang, Y.; Bao, X. A Comparative Study of Intercalation Mechanism at Graphene/Ru(0001) Interface. *Surf. Sci.* **2013**, *617*, 81−86.
(41) Petrović, M.; Rakić, I. Š.; Runte, S.; Busse, C.; Sadowski, J. T.; Lazić, P.; Pletikosić, I.; Pan, Z.-H.; Milun, M.; Pervan, P.; et al. The Mechanism of Caesium Intercalation of Graphene. *Nat. Commun.* **2013**, *4*, 2772.
(42) Graupner, R.; Hollering, M.; Ziegler, A.; Ristein, J.; Ley, L.; Stampfl, A. Dispersions of Surface States on Diamond (100) and (111). *Phys. Rev. B: Condens. Matter Mater. Phys.* **1997**, *55*, 10841−10847.
(43) Himpsel, F. J.; Eastman, D. E.; Heimann, P.; van der Veen, J. F. Surface States on Reconstructed Diamond (111). *Phys. Rev. B: Condens. Matter Mater. Phys.* **1981**, *24*, 7270−7274.
(44) Himpsel, F. J.; van der Veen, J. F.; Eastman, D. E. Experimental bulk energy bands for diamond usinghν-dependent photoemission. *Phys. Rev. B: Condens. Matter Mater. Phys.* **1980**, *22*, 1967−1971.
(45) Mathieu, C.; Barrett, N.; Rault, J.; Mi, Y. Y.; Zhang, B.; de Heer, W. A.; Berger, C.; Conrad, E. H.; Renault, O. Microscopic Correlation between Chemical and Electronic States in Epitaxial Graphene on SiC (0001). *Phys. Rev. B: Condens. Matter Mater. Phys.* **2011**, *83*, 235436.
(46) Nguyen, T. H.; Perilli, D.; Cattelan, M.; Liu, H.; Sedona, F.; Fox, N. A.; Di Valentin, C.; Agnoli, S. Microscopic Insight into the Single Step Growth of In-Plane Heterostructures between Graphene and Hexagonal Boron Nitride. *Nano Res.* **2019**, *12*, 1−8.
(47) Wang, F.; Liu, G.; Rothwell, S.; Nevius, M. S.; Mathieu, C.; Barrett, N.; Sala, A.; Menteş, T. O.; Locatelli, A.; Cohen, P. I.; et al. Pattern Induced Ordering of Semiconducting Graphene Ribbons Grown from Nitrogen-Seeded SiC. *Carbon* **2015**, *82*, 360−367.
(48) Zamborlini, G.; Lüftner, D.; Feng, Z.; Kollmann, B.; Puschnig, P.; Dri, C.; Panighel, M.; Di Santo, G.; Goldoni, A.; Comelli, G.; et al. Multi-Orbital Charge Transfer at Highly Oriented Organic/Metal Interfaces. *Nat. Commun.* **2017**, *8*, 335.
(49) Barrett, N.; Gottlob, D. M.; Mathieu, C.; Lubin, C.; Passicousset, J.; Renault, O.; Martinez, E. Operando X-Ray Photoelectron Emission Microscopy for Studying Forward and Reverse Biased Silicon p-n Junctions. *Rev. Sci. Instrum.* **2016**, *87*, 053703.
(50) Man, M. K. L.; Margiolakis, A.; Deckoff-Jones, S.; Harada, T.; Wong, E. L.; Krishna, M. B. M.; Madéo, J.; Winchester, A.; Lei, S.; Vajtai, R.; et al. Imaging the Motion of Electrons across Semiconductor Heterojunctions. *Nat. Nanotechnol.* **2016**, *12*, 36−40.
(51) Müller, K.; Burkov, Y.; Schmeiβer, D. Photo-Emission-Electron-Microscopy for Characterization of an Operating Organic Electronic Device. *Thin Solid Films* **2006**, *495*, 219−223.
(52) Wang, Y.; Ding, Y.; Ni, J. Electronic Structures of Fe-Terminated Armchair Boron Nitride Nanoribbons. *Appl. Phys. Lett.* **2011**, *99*, 053123.
(53) Xuan, Y.; Lin, H.-C.; Ye, P. D. Simplified Surface Preparation for GaAs Passivation Using Atomic Layer-Deposited High- k Dielectrics. *IEEE Trans. Electron Devices* **2007**, *54*, 1811−1817.
(54) Machuca, F.; Liu, Z.; Sun, Y.; Pianetta, P.; Spicer, W. E.; Pease, R. F. W. Oxygen Species in Cs/O Activated Gallium Nitride (GaN) Negative Electron Affinity Photocathodes. *J. Vac. Sci. Technol., B: Microelectron. Nanometer Struct.* **2003**, *21*, 1863.
(55) Perdew, J. P.; Burke, K.; Ernzerhof, M. Generalized Gradient Approximation Made Simple. *Phys. Rev. Lett.* **1996**, *77*, 3865−3868.
(56) Clark, S. J.; Segall, M. D.; Pickard, C. J.; Hasnip, P. J.; Probert, M. I. J.; Refson, K.; Payne, M. C. First Principles Methods Using CASTEP. *Z. für Kristallogr.—Cryst. Mater.* **2005**, *220*, 567−570.
(57) Vanderbilt, D. Soft Self-Consistent Pseudopotentials in a Generalized Eigenvalue Formalism. *Phys. Rev. B: Condens. Matter Mater. Phys.* **1990**, *41*, 7892−7895.
(58) Pack, J. D.; Monkhorst, H. J. "Special Points for Brillouin-Zone Integrations"—a Reply. *Phys. Rev. B: Condens. Matter Mater. Phys.* **1977**, *16*, 1748−1749.
(59) Mucha, J. A.; Flamm, D. L.; Ibbotson, D. E. On the role of oxygen and hydrogen in diamond-forming discharges. *J. Appl. Phys.* **1989**, *65*, 3448−3452.
(60) Tallaire, A.; Achard, J.; Silva, F.; Sussmann, R. S.; Gicquel, A.; Rzepka, E. Oxygen Plasma Pre-Treatments for High Quality Homoepitaxial CVD Diamond Deposition. *Phys. Status Solidi A* **2004**, *201*, 2419−2424.
(61) Joshi, A.; Nimmagadda, R. Erosion of Diamond Films and Graphite in Oxygen Plasma. *J. Mater. Res.* **2011**, *6*, 1484−1490.
(62) Grogan, D. F.; Zhao, T.; Bovard, B. G.; Macleod, H. A. Planarizing Technique for Ion-Beam Polishing of Diamond Films. *Appl. Opt.* **1992**, *31*, 1483.
(63) Shpilman, Z.; Gouzman, I.; Grossman, E.; Akhvlediani, R.; Hoffman, A. Oxidation of Diamond Films by Atomic Oxygen: High

DOI: 10.1021/acs.jpcc.8b11232
J. Phys. Chem. C 2019, 123, 4168−4177

Resolution Electron Energy Loss Spectroscopy Studies. *J. Appl. Phys.* **2007**, *102*, 114914.
(64) Ghodbane, S.; Ballutaud, D.; Deneuville, A.; Baron, C. Influence of Boron Concentration on the XPS Spectra of the (100) Surface of Homoepitaxial Boron-Doped Diamond Films. *Phys. Status Solidi A* **2006**, *203*, 3147−3151.
(65) Ren, B.; Huang, J.; Yu, H.; Yang, W.; Wang, L.; Pan, Z.; Wang, L. Thermal Stability of Hydrogenated Diamond Films in Nitrogen Ambience Studied by Reflection Electron Energy Spectroscopy and X-Ray Photoelectron Spectroscopy. *Appl. Surf. Sci.* **2016**, *388*, 565−570.
(66) Klauser, R.; Chen, J.-M.; Chuang, T. J.; Chen, L. M.; Shih, M. C.; Lin, J.-C. The Interaction of Oxygen and Hydrogen on a Diamond C(111) Surface: A Synchrotron Radiation Photoemission, LEED and AES Study. *Surf. Sci.* **1996**, *356*, L410−L416.
(67) Park, Y.; Choong, V.; Gao, Y.; Hsieh, B. R.; Tang, C. W. Work Function of Indium Tin Oxide Transparent Conductor Measured by Photoelectron Spectroscopy. *Appl. Phys. Lett.* **1996**, *68*, 2699−2701.
(68) Diederich, L.; Küttel, O. M.; Schaller, E.; Schlapbach, L. Photoemission from the Negative Electron Affinity (100) Natural Hydrogen Terminated Diamond Surface. *Surf. Sci.* **1996**, *349*, 176−184.
(69) Clark, C. D.; Dean, P. J.; Harris, P. V. Intrinsic Edge Absorption in Diamond. *Proc. Roy. Soc. Lond. Math. Phys. Sci.* **1964**, *277*, 312−329.
(70) Cui, J. B.; Graupner, R.; Ristein, J.; Ley, L. Electron Affinity and Band Bending of Single Crystal Diamond (111) Surface. *Diamond Relat. Mater.* **1999**, *8*, 748−753.
(71) Wallauer, R.; Reimann, J.; Armbrust, N.; Güdde, J.; Höfer, U. Intervalley Scattering in MoS2 Imaged by Two-Photon Photoemission with a High-Harmonic Probe. *Appl. Phys. Lett.* **2016**, *109*, 162102.
(72) Zhang, Y.; Chang, T.-R.; Zhou, B.; Cui, Y.-T.; Yan, H.; Liu, Z.; Schmitt, F.; Lee, J.; Moore, R.; Chen, Y.; et al. Direct Observation of the Transition from Indirect to Direct Bandgap in Atomically Thin Epitaxial MoSe2. *Nat. Nanotechnol.* **2013**, *9*, 111−115.
(73) Yuan, H.; Liu, Z.; Xu, G.; Zhou, B.; Wu, S.; Dumcenco, D.; Yan, K.; Zhang, Y.; Mo, S.-K.; Dudin, P.; et al. Evolution of the Valley Position in Bulk Transition-Metal Chalcogenides and Their Monolayer Limit. *Nano Lett.* **2016**, *16*, 4738−4745.
(74) Dean, P. J.; Lightowlers, E. C.; Wight, D. R. Intrinsic and Extrinsic Recombination Radiation from Natural and Synthetic Aluminum-Doped Diamond. *Phys. Rev.* **1965**, *140*, A352−A368.
(75) Bandis, C.; Pate, B. B. Photoelectric Emission from Negative-Electron-Affinity Diamond (111) Surfaces: Exciton Breakup versus Conduction-Band Emission. *Phys. Rev. B: Condens. Matter Mater. Phys.* **1995**, *52*, 12056−12071.
(76) Willatzen, M.; Cardona, M.; Christensen, N. E. Linear muffin-tin-orbital andk·pcalculations of effective masses and band structure of semiconducting diamond. *Phys. Rev. B: Condens. Matter Mater. Phys.* **1994**, *50*, 18054−18059.
(77) Pehrsson, P. E.; Mercer, T. W. Oxidation of the Hydrogenated Diamond (100) Surface. *Surf. Sci.* **2000**, *460*, 49−66.
(78) Derry, T. E.; Makau, N. W.; Stampfl, C. Oxygen adsorption on the (1 × 1) and (2 × 1) reconstructed C(111) surfaces: a density functional theory study. *J. Phys.: Condens. Matter* **2010**, *22*, 265007.
(79) Thomas, R. E.; Rudder, R. A.; Markunas, R. J. Thermal Desorption from Hydrogenated and Oxygenated Diamond (100) Surfaces. *J. Vac. Sci. Technol., A* **1992**, *10*, 2451−2457.

DOI: 10.1021/acs.jpcc.8b11232
J. Phys. Chem. C 2019, 123, 4168−4177